Hard x-ray methods for studying the structure of amorphous thin films and bulk glassy oxides

C J Benmore[1,2,*] **, G B González**[3] **, O L G Alderman**[4] **, S K Wilke**[5] **, J L Yarger**[2] **, K Leinenweber**[2] **and J K R Weber**[1,5]

[1] X-Ray Science Division, Advanced Photon Source, Argonne National Laboratory, Argonne, IL 60439, United States of America
[2] Arizona State University, Tempe, AZ 85287, United States of America
[3] Department of Physics, DePaul University, Chicago, Illinois 60614, United States of America
[4] ISIS Neutron and Muon Source, Science and Technology Facilities Council, Rutherford Appleton Laboratory, Harwell Campus, Didcot OX11 0QX, United Kingdom
[5] Materials Development, Inc., Evanston, IL 60202, United States of America

E-mail: benmore@anl.gov

CrossMark

Abstract

High-energy photon diffraction minimizes many of the corrections associated with laboratory x-ray diffractometers, and enables structure factor measurements to be made over a wide range of momentum transfers. The method edges us closer toward an ideal experiment, in which coordination numbers can be extracted without knowledge of the sample density. Three case studies are presented that demonstrate new hard x-ray methods for studying the structure of glassy and amorphous materials. First, the methodology and analysis of high-energy grazing incidence on thin films is discussed for the case of amorphous In_2O_3. The connectivity of irregular InO_6 polyhedra are shown to exist in face-, edge- and corner-shared configurations in the approximate ratio of 1:2:3. Secondly, the technique of high-energy small and wide angle scattering has been carried out on laser heated and aerodynamically levitated samples of silica-rich barium silicate ($20BaO:80SiO_2$), from the single phase melt at 1500 ℃ to the phase separated glass at room temperature. Based on Ba–O coordination numbers of 6 to 7, it is argued that the although the potential of Ba is ionic, it is weak enough to cause the liquid–liquid immiscibility to become metastable. Lastly, high-energy small and wide angle scattering has also been applied to high water content (up to 12 wt.%) samples of hydrous SiO_2 glass quenched from 1500 ℃ at 4 GPa. An increase of $Si_1–O_2$ correlations at 4.3 Å is found to be consistent with an increase in the population of three-membered SiO_4 rings at the expense of larger rings.

Keywords: x-ray diffraction, pair distribution function, liquids and glasses, coordination numbers

(Some figures may appear in colour only in the online journal)

1. Introduction

The idea that multicomponent oxide glass structures are not homogenous, but in fact are made up of a modified random network in which cations form percolation channels running throughout a glassy network can be attributed to the pioneering work of Prof. Neville Greaves (Greaves *et al* 1981, Greaves 1985, Greaves and Sen 2007). This breakthrough underscored the need to probe amorphous and glassy structures at both the atomic and nanometer length-scales, to understand the

relationship between local and intermediate range ordering. The pair distribution function (PDF) technique is well suited to these investigations, and with the advent of high flux, high-energy photons over the past two decades, this has led to the widespread use of the x-ray PDF technique for the study of disordered materials. Nowadays, chemists often use x-ray PDF to follow time-resolved reactions, with changing compositions and multiple crystalline forms, to obtain useful qualitative information on the local disorder and evolving nanometer topologies. However, physicists studying liquid, glassy and amorphous materials still need to invoke a rigorous consideration of the data analysis corrections and normalization procedures, required to obtain quantitative information such as coordination numbers, and provide an accurate comparison to molecular dynamics simulations.

Here we address some of the issues associated with x-ray PDF in the context of thin film amorphous and bulk glassy oxides using *new* hard x-ray synchrotron methods. In particular, the relationship between the PDF, density and coordination number are considered. These are described in detail in the next section, and the rest of the paper organized in the following way: three examples are presented, ranging from the grazing incidence PDF measurements of amorphous thin films, to SAXS/WAXS measurements of bulk oxide glasses synthesized from liquids at high temperatures and high pressures. The latter examples build on existing synchrotron SAXS/WAXS techniques for studying the local structures and nanoscale inhomogeneities in glass (Bras *et al* 2003). Finally, a brief outlook is presented with a view to enabling the exploration of both equilibrium and metastable phase diagrams.

1.1. Normalization and coordination numbers

The extraction of coordination numbers from the first few peaks in the real space PDF are typically performed by integration between minima either side of a peak, or by a full Gaussian peak fit (Waseda 1980). This can be achieved for x-rays provided the Q-dependence of the weighting factors and truncation effects are taken into account (Keen 2001, Pickup *et al* 2014). However, in practice the normalization of laboratory based x-ray diffraction data can be problematic due to uncertainties in sample, and source dependent corrections (Levy *et al* 1966). To overcome this the Krogh-Moe-Norman normalization method is often employed, which uses the sum-rule relation in the unphysical region, below the first true peak in the PDF, based on knowledge of the density of the sample (Krogh-Moe 1956, Norman 1957). Care should be taken here however, because as Wright (Wright 1994) has pointed out, this region of the PDF also contains information on systematic errors in the experiment and obscuring it hides the true quality of the measured data. The situation improves with the use of high-energy photons at synchrotrons, which minimize the attenuation and multiple scattering corrections and enable access to high momentum transfers. However, synchrotron data is still subject to small inaccuracies, primarily due to detector related corrections (Skinner *et al* 2012). Consequently, quantitative x-ray analysis software (Qiu *et al* 2004a, Soper and Barney 2011) and modeling methods (McGreevy and Pusztai 1988, Soper

2005) require an accurate knowledge of *both* the composition and the density to obtain meaningful local coordination numbers from PDF data. For this reason the local structure is often interpreted by analogy to crystalline phases or on the basis of ionic radii (Dippel *et al* 2019, Jensen *et al* 2015).

Although the material density is needed for calculating attenuation and multiple scattering factors, for x-rays these effects diminish drastically at high energies, $E > 60$ keV (Benmore 2012a). Consequently, provided the sample composition is known and can be verified by comparing the sample intensity to x-ray self-scattering, i.e., the composition weighted form factors plus Compton scattering, the local coordination numbers can be extracted by fitting Gaussian atom–atom correlations to the high Q-part of the total x-ray structure factor using the Debye scattering formula (Warren 1990, Narten 1972).

$$S(Q) = \sum_{i,j=1}^{n} \frac{N_{ij} c_i f_i(Q) f_j(Q)}{\left[\sum_{i=1}^{n} c_i f_i(Q)\right]^2} \text{sinc}\left(Q r_{ij}\right) \exp(-Q^2 \sigma^2{}_{ij}/2),$$

(1)

where N_{ij}, r_{ij} and σ_{ij} represent the coordination number, atomic separation and disorder parameter of atoms of species i relative to species j. c_i and $f_i(Q)$ represent the concentration and Q-dependent x-ray atomic form factor of species i. This is because the Sine Fourier transform from $S(Q) - 1$ to the differential distribution function $D(r)$, using the Hannon–Howells–Soper formalism (Keen 2001), does not require knowledge of the atomic number density, ρ, and this is the focus of the peak fit procedure in equation (1). In contrast, the integral of $rT(r) = rD(r) + 4\pi\rho r^2$ which is the more conventional method of extracting the coordination number directly from the PDF in glasses, does contain a density dependence. This underscores to an important point. Namely, if high-energy x-ray data can be accurately normalized to the number of electrons in the sample at high-Q values, coordination numbers can be extracted without knowledge of the density. In this '*perfect case*' the exact sample composition and normalization of the scattered x-ray intensity is required. For amorphous and glassy materials the latter requires a careful application of standard corrections (Qiu *et al* 2004a, Soper and Barney 2011). To illustrate this point, in figure 1 we show the measured x-ray structure factor for glassy SiO_2, compared to manufactured x-ray diffraction patterns that have been Fourier filtered to correspond to different local coordination numbers. Here the Fourier filtered PDF's are kept the same as the measured function for distances longer than the first (Si–O) peak, denoted by r_{cut}, but the Si–O peak (below r_{cut}) is replaced by equation (1) with N_{Si-O} set to values of 3, 4 and 5. The corresponding Fourier filtered x-ray structure factors show the level of sensitivity required across the entire Q-range, compared to the measured $S(Q)$.

There are of course caveats to fitting Gaussians in Q-space. For liquid and glassy materials the coordination numbers of heavier cations are significantly smaller and their bond length distributions more asymmetric than their crystalline counterparts, which may require multiple Gaussian fitting to describe specific cation–oxygen interactions (Skinner *et al* 2014). Ultimately the efficacy of these methods depends on how accurately the sample $S_X(Q)$ can be extracted and the partial pair
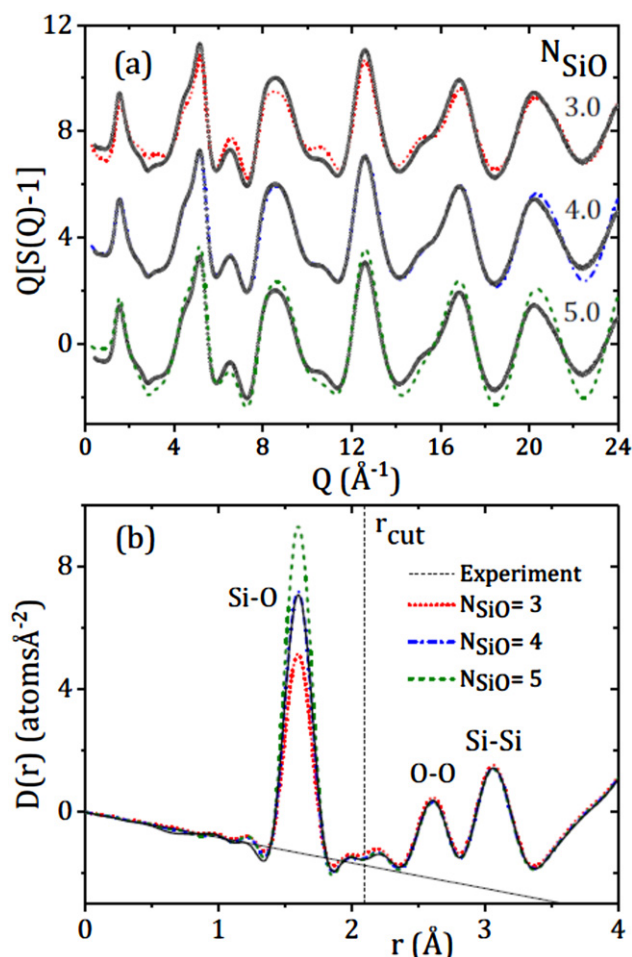
Figure 1. (a) The measured x-ray total structure factor for SiO_2 glass (black circles) compared to Fourier filtered structure factors with local coordination numbers of 3 (red dotted line), 4 (blue dash-dot lined) and 5 (green dashed line). (b) The corresponding x-ray differential pair distribution functions.

weighting factors for a particular sample, but it nonetheless underlines the need for a careful application of the corrections. Here we apply these methods to three different high-energy x-ray measurements on liquid, glassy and amorphous materials. Namely, grazing incidence experiments on thin films and small and wide angle scattering (SAXS/WAXS) measurements on high temperature liquids and glasses quenched at high pressures.

2. Grazing incidence-pair distribution function (GI–PDF) measurements

The advent of high-energy, wide angle x-ray scattering, for GI-PDF measurements (Dippel *et al* 2019), represents a new and powerful technique for investigating the structure of disordered, nanometer-sized thin films, which are not feasible in transmission geometry. The GI-WAXS signal ($2\theta > 5°$) is far from the critical angle and thereby satisfactorily described by the Born approximation (Sinha *et al* 1988). It has been estimated that grazing incidence geometries have reduced the

minimum detectable thin film thickness by one order of magnitude compared to transmission geometry (Dippel *et al* 2019). Indium oxide films can be grown on amorphous silica substrates using pulsed laser deposition by varying the film growth temperature. The electrical and optical properties of indium oxide films are strongly influenced by both their oxygen content and their structural phase (Buchholz *et al* 2013, 2014). Indeed, amorphous thin films are often preferable to crystalline films but are of unknown or variable density, whose structures can vary depending on the deposition conditions (Dippel *et al* 2019, Jensen *et al* 2015, González *et al* 2017). The metal cations can also form a distribution of coordination polyhedral, with connectivities that are not present in the crystalline forms. In a bixbyite type crystal structure such as In_2O_3, InO_X polyhedra typically corner share through bridging oxygens or at their edges where two oxygens are shared between adjacent polyhedra.

2.1. Grazing incidence experiment

Scattering from amorphous In_2O_3 (<1 μm thick) thin films deposited on a SiO_2 substrate were measured using beamline 1-ID at the Advanced Photon Source, using grazing incidence geometry with 70 keV x-rays at an incident angle α of 0.04°. The diffraction patterns were collected with a 2D a-Si area general electric detector with 2048 × 2048 pixels (pixel size of 200 μm × 200 μm) at a distance of 325 mm away from the sample. The sample horizon divides the scattered image, with the upper part reaching the detector only attenuated by air and the lower part attenuated by the length of the sample substrate as described by (Dippel *et al* 2019). The in-plane data were integrated to 10° above the horizon and corrected for flat field, polarization, rotation and tilt using the *GSAS-II* software (Toby and Von Dreele 2013). The program *PDFgetX2* (Qiu *et al* 2004b) was used to correct for background, oblique incidence, absorption and detector efficiency effects as described in (Skinner *et al* 2012). As can be seen in figure 2 the raw signal from the SiO_2 substrate is substantially larger than the thin film scattering. We note that there are (at least) two parts to the background in this type of experiment; namely the air scatter and the substrate scatter. The air scatter is invariant, and can be subtracted directly. The substrate scatter may be subject to slightly different path lengths as illustrated in the figure 2 insert, depending on the accuracy of the re-positioning and thickness of the film or penetration depth. In this case a small (~1%) scaling of the scattering angle axis was required to approximate the slight shift in the substrate scattering. This factor was calculated from the slight change in the Si–O bond length at ~1.6 Å obtained through a Fourier transform to $D(r)$. The degraded Q-space resolution due to the large x-ray path length through the sample in GI geometry compared to conventional transmission geometry of SiO_2 was also readily apparent.

2.2. Grazing incidence results and discussion

The normalized electronic scattering intensity from the amorphous In_2O_3 thin film is shown in figure 3(a) compared to
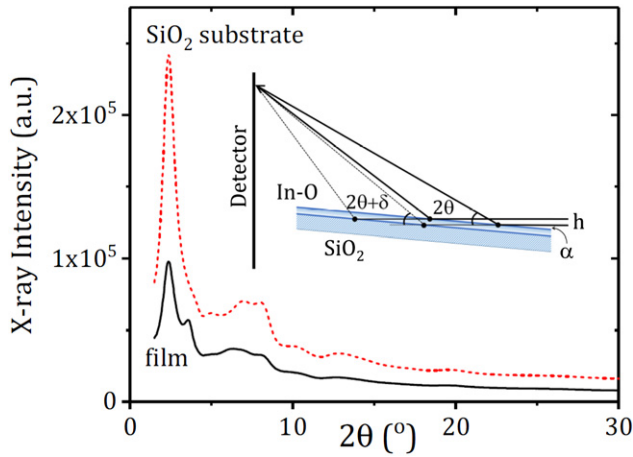
Figure 2. The x-ray intensity of the thin film (solid black line) and SiO_2 substrate (red dotted black line) as a function of scattering angle. The insert illustrates how grazing incidence geometry is susceptible to small offsets in the scattering angle for a beam of height h incident at an angle α to the film.

Figure 3. (a) The normalized electronic scattering intensity from the amorphous In_2O_3 thin film compared to the published data for amorphous In_2O_3 (Utsuno *et al* 2006). (b) The corresponding pseudo-nuclear total x-ray structure factor (black circles) and the contributions from the fitted In–O (red dashed line) and In–In (green dotted line) coordination shells.

published GI data (Utsuno *et al* 2006). The x-ray diffraction patterns are quantitatively very similar, but the high-Q region for a-In_2O_3 in this high-energy experiment has much better statistics. A steep rise toward the lowest Q-values indicates that the local density of the sample is heterogeneous on the scale of a few nanometers. The corresponding pseudo-nuclear structure factor is shown in figure 3(b) together with the contributions from the In–O and In–In fits, whose correlations dominate the measured GI pattern. Here we use the term 'pseudo-nuclear' previously coined by Egelstaff (Egelstaff 1983) to acknowledge the fact that x-rays scatter from electrons (not the nucleus) and a deconvolution of a spherical electron cloud is performed in the analysis to estimate the nuclear center. The In–O and In–In coordination environments were obtained using the method described in the section above, see also (Pickup *et al* 2014). The r_{ij} and σ_{ij} were extracted from $D(r)$, and N_{ij} is scaled to the correct magnitude compared to the experimental $S(Q)$. These parameters and the density were refined by iterating parameters between Q and r-space. The In-O coordination number was best fit with two Gaussians to account for the long high-r asymmetric tail with $N_{In-O} = 4.3$ at 2.03 Å and $N_{In-O} = 1.7$ at 2.28 Å, yielding a total of $N_{In-O} = 6.0 \pm 0.5$. The In–O coordination number in this study is in agreement with the value of $N_{In-O} \sim 6$ at an average distance of 2.12 Å in amorphous In_2O_3 (Utsuno *et al* 2006). However, the first average peak position in $D(r)$ for amorphous In_2O_3 is at 2.06 Å, which is shorter than the 2.18 Å found for InO_6 in the bixbyite structure, indicating distortion of the polyhedra, or a distribution of coordination numbers with some indium bonded to less, and some to more, than six oxygens. Moreover, the density of the film extracted from the unphysical low-r region corresponds to 4.61 g cm^{-3} which is substantially lower than bixbyite In_2O_3 (7.2 g cm^{-3}). Errors on the In-O coordination number and density are likely slightly larger than the typical $\pm5\%$ (Skinner *et al* 2014) due to the poor Q-space resolution associated with GI geometry.
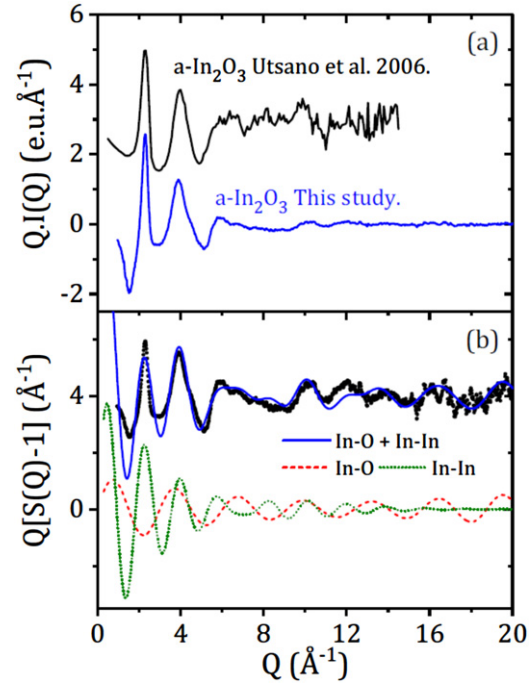
The corresponding differential distribution function for amorphous In_2O_3 is shown in figure 4. The low density and large local distortion of the six fold polyhedra strongly influences the connectivity of InO_6 polyhedra. In crystalline In_2O_3 there are an equal number of corner and edge shared octahedra giving rise to In–In distances of around 3.5 Å. For our amorphous GI–PDF, at least three peaks are required to fit the connectivity of adjacent InO_6 polyhedra. We note that the contribution from O–O correlations corresponding to $N_{OO} = 5.5$ at ~2.70 Å was also fitted, but it's contribution was found to be negligible due to the small x-ray pair weighting factor. The three In–In peaks shown in figure 4 correspond to $N_{InIn} = 1.8$ In atoms at 2.69 Å (face-sharing from the longer In–O bonds of the irregular InO_6 octahedra), $N_{InIn} = 3.7$ at 3.28 Å (edge-sharing) and $N_{InIn} = 5.9$ at 3.72 Å (corner-sharing). The fitting of the In-In corner-sharing peak is subject to some uncertainty due to overlap at high-r, but the approximate ratio of face:edge:corner sharing of distorted InO_6 polyhedra corresponds to 1:2:3 (compared to 0:1:1 in bixbyite). Previous molecular dynamics simulations and Reverse Monte Carlo fits to a-In_2O_3 did not allow any face-sharing polyhedra, but failed to fit the measured intensity in the GI–PDF around 2.7 Å. Although, we recognize that texture is a common phenomenon in thin films and the amorphous structure itself may also vary with azimuthal angle along a Debye–Scherrer ring. Finally, the face, edge and corner-sharing In-In peak fits are found to yield average $\angle$In–O–In angles of 82°, 106° and 129°. These compare to 100° (edge) and 123° (corner) in bixbyite (Buchholz *et al* 2014).
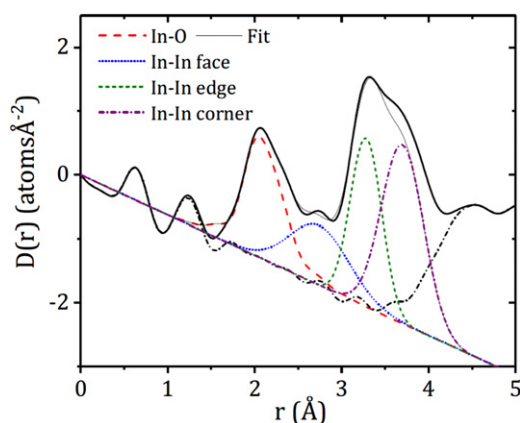
Figure 4. $D(r)$ for amorphous In_2O_3 (solid black line) and the In−O and In−In peak fits described in the text (sum shown as thin solid line).

3. High temperature SAXS/WAXS

Several binary silicate systems phase separate into two liquids in the silica-rich region of the phase diagram. Generally, a highly polymerized silicate network separates from a cation-rich structure that satisfies the modifying atoms' coordination requirements. The widths of these immiscibility gaps have been shown to change according to ionic potential and the cation coordination number. Hudon and Baker (Hudon and Baker 2002) reviewed 41 binary systems and characterized them into groups. The majority can be placed in either of two groups: (i) network modifying cations with a large ionic radius and coordination number $\geqslant 5$ e.g. Ba. These cations are surrounded by both bridging and non-bridging oxygens which can screen their positive charges. However, bridging oxygens provide poor shielding compared to non-bridging oxygens, because they have strong covalent bonds to the Si. This results in substantial Coulombic repulsions between network modifying cations that is the primary origin of phase separation. (ii) Cations with small ionic radii that possess a significant number of four-fold coordinated cations as well as higher coordinated cations. The four-fold cations are able to form covalent bonds and can be incorporated into the polymerized silica-rich network, whereas the larger coordinate species lead to phase separation. This mixture of covalent and ionic bonding types can lead to metastable immiscibility e.g. in the Al_2O_3−SiO_2 system.

The BaO−SiO₂ system has an upper consulate temperature of 1460 °C (Zanotto *et al* 1986) and is of interest because although it has a metastable immiscibility gap (Seward *et al* 1968), it has the least covalent character of the alkaline-earth divalent cations. Indeed, based on the electronegativity scale, BaO < SrO < CaO < MgO (Pacchioni and Illas 1995) and in the BaO crystalline phase Ba has a coordination number of 6 with an ionic character, increasing up to 9.5 in Ba_2SiO_4 (Rai and Mountjoy 2014). There are only a few structural studies of $xBaO_{(1-x)}SiO_2$ using diffraction methods and these have concentrated on the single-phase glass forming region with $x = 33.3$ and 40 (Hasegawa and Yasui 1987, Cormier *et al* 1999). Molecular dynamics modeling over this composition

range predicts a polymerized silicate network incorporating 6 to seven-fold coordinated barium.

3.1. High temperature experiment

Details of the aerodynamic levitation and laser heating system have been described in previous publications (Weber *et al* 2014, Benmore and Weber 2017). Here, 2–3 mm diameter spheres of 20BaO−80SiO₂ were prepared with masses ranging from 24–28 mg. Levitation was achieved by flowing an upward stream of high purity O₂ gas through a divergent nozzle, and the samples heated from above with a 400 W CO₂ laser (Firestar i401, Synrad Inc.). An optical pyrometer (IR-CAS Chino) was used to measure the apparent surface temperature of the heated samples and a spectral emissivity correction of 1.01 was applied. The pyrometer measurement, x-ray beam and laser were all coincident within a ∼0.2 mm region at the top of the sample. Due to the fast evaporation rate of silica at high temperatures, short experiments of 10 s were performed, limiting the mass loss during the experiments to <0.5%, thus ensuring only small compositional changes. The samples were cooled at a rate of ∼200 °C s⁻¹ from the high temperature stable liquid and recovered as glass.

We have performed simultaneous high-energy SAXS/WAXS measurements on liquid and glassy 20BaO−80SiO₂ on beamline 6-ID-D at the APS in transmission geometry, using an incident energy of 80.2 keV. Details of the set up have been described previously (Benmore *et al* 2020b, 2020a) so will only be briefly outlined here. Two Dexela 2315-MAM detectors with sample to detector distances of ∼28 cm and ∼230 cm provided a continuous Q-range from ∼0.025 to ∼19 Å⁻¹ with an overlap region of $\Delta Q \sim 2$ Å⁻¹. The SAXS detector diffraction patterns were calibrated using silver behenate and the WAXS detector with a NIST CeO₂ standard. Brass sheets of 0.5 mm thickness were placed in front of each detector to reduce the Ba fluorescence from the sample. Both data sets were analyzed using the *Fit2D* software (Hammersley 2016) and corrected for flat field, polarization, rotation and tilt and spliced together at $Q \sim 0.9$ Å⁻¹, see figure 5. The program *PDFgetX2* (Qiu *et al* 2004b) was used to correct for background, oblique incidence, absorption and detector efficiency effects and normalize the WAXS, $I(Q)$, data to the sample self-scattering in absolute electron units. It is important to note that the brass sheets left a residual fluorescence background which was subtracted empirically by normalizing to the Si−O peak at 1.6 Å in the glass (assuming SiO₄ tetrahedra) using an iterative process. Similar parameters were used for the liquid and maintaining the requirement that $S(Q)$ has to oscillate about 1. This analysis yielded an approximate density of 2.6 g cm⁻³, which lies between that of glassy silica (2.2 g cm⁻³) and the single phase glass 25BaO−75SiO₂ (3.33 g cm⁻³) (Rai and Mountjoy 2014). The density used here is significantly lower (13%) than the 2.93(9) g cm⁻³ reported by (Tomlinson *et al* 1958) for molten 20BaO−80SiO₂ at 1700 °C. The extracted total x-ray structure factor, S(Q) (see figure 6), was truncated at a maximum Q-value, corresponding to a positive node at $Q \sim 17.5$ Å⁻¹, and Fourier transformed using a Lorch modification
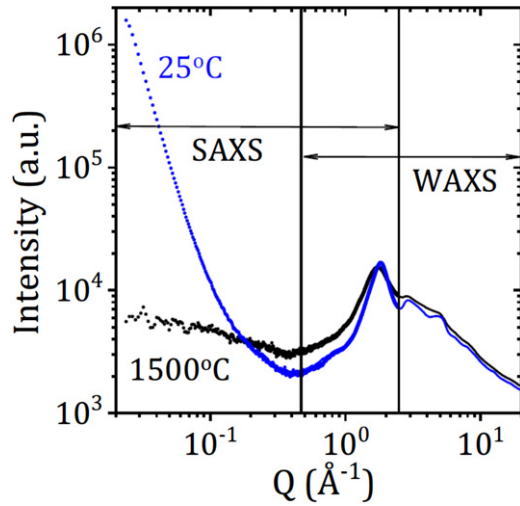
Figure 5. Comparison of the simultaneously measured SAXS and WAXS intensities of 20BaO–80SiO$_2$ for the high temperature liquid and quenched glass at room temperature.
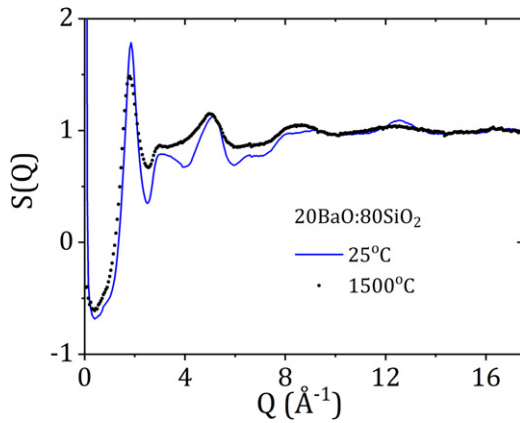

Figure 6. The x-ray total structure factors for the high temperature supercooled liquid and room temperature glassy 20BaO:80SiO$_2$.

function to minimize truncation ripples and yield $D(r)$, see figure 7.

Porod index from the SAXS I(Q) data shown in figure 5(b) increases from 0.3 at ~1500 °C to 3.56 at 25 °C indicating miscibility in the high temperature supercooled liquid, but a smooth interface between the phase separated components in the glassy phase. These changes are concomitant with a considerable sharpening of the peaks in the glassy $S(Q)$ shown in figure 6, indicating a considerably more ordered structure.

3.2. High temperature results and discussion

The x-ray differential PDF for the single-phase high temperature 20BaO:80SiO$_2$ liquid shows broad overlapping peaks beyond the nearest neighbor Si–O peak. This includes a slight asymmetry around 1.76 Å indicative of long Si–O bonds (Shannon and Prewitt 1970), which are not present in the room temperature glass. This feature and the peaks at longer distances were interpreted based on the classical molecular dynamics simulations (MD) of (Rai and Mountjoy 2014),
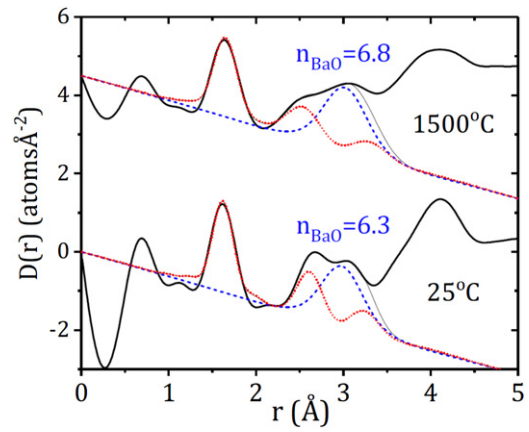

Figure 7. The x-ray differential distribution function, $D(r)$, for the high temperature supercooled liquid and room temperature glassy 20BaO:80SiO$_2$ (thick solid black line) compared to the sum of peak fits (thin solid black line). The sum of the Si–O, O–O and Si–Si peaks are shown by the dotted red line, and the Ba–O peak is represented by the blue dashed line.

which have been performed on single phase xBaO$_{(1-x)}$SiO$_2$ glasses using Teter inter-atomic potentials for $x \geqslant 33.3$. We have also performed preliminary MD NPT simulations on the quenched liquid 20BaO:80SiO$_2$ using these potentials but found the Si–O coordination to be 4 only throughout the quench from liquid to glass. The Si–O (1.6 Å), O–O (2.6 Å) and Si–Si (3.1 Å) peaks associated with a polymerized silica network sharpen as the system phase separates. The broader Ba–O peak is centered at ~3.0 Å. At longer distances the first Ba–Ba peak in the molecular dynamics simulation is at 4.2 Å, and the first Ba–Si peak is around 3.8 Å. The fitted Ba–O coordination number reduces from 6.8(5) in the melt to 6.3(3) in the barium-rich component of the glass. This compares to a Ba–O coordination number of 6.8 for $x = 33.3$ from MD (Rai and Mountjoy 2014). A mixture model of this barium silicate glass (digitized from the MD model of (Rai and Mountjoy 2014)) was combined with the PDF of pure silica in a ratio of 77:23. The mixture model qualitatively reproduces the measured features observed in the two-phase 20BaO:80SiO$_2$ glass differential PDF, $D(r)$ in figure 8.

Neither, our data, the MD simulations (Rai and Mountjoy 2014) or neutron experiments (Hasegawa and Yasui 1987) indicate evidence of a significant amount of four-fold Ba as the source of the metastable phase separation. Rather, we note that Ba has a very weak ionic potential, which greatly reduces the Coulombic repulsion and the width of the resulting miscibility gap. So, we argue that provided the Ba cations are coordinated by a sufficient number of non-bridging oxygens in less polymerized regions of the melt, the repulsions between them can be neutralized. The broad peaks in $D(r)$ for the single phase 20BaO:80SiO$_2$ melt, compared to the sharp silica network (O–O and Si–Si) peaks observed in the phase separated glass supports this assertion [bearing in mind that pure SiO$_2$ also has sharp peaks in the liquid state (Skinner *et al* 2013)]. This indicates that it is the weak ionic potential of Ba which is the origin of metastable liquid–liquid immiscibility in the BaO–SiO$_2$ system.
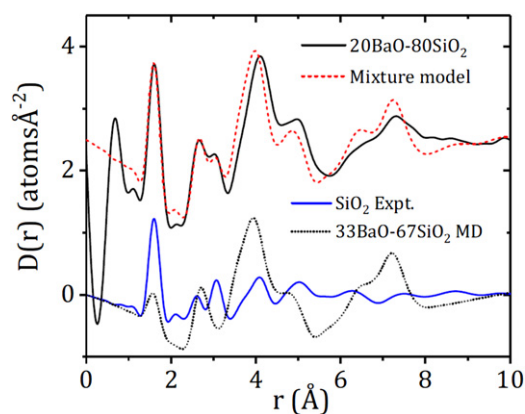
Figure 8. The differential distribution function, $D(r)$, for phase separated $20BaO:80SiO_2$ glass (solid black line) compared to a mixture model (red dashed line). Below are the two components of the mixture model; SiO_2 glass (blue solid line) and molecular dynamics simulation of single phase $33BaO:67SiO_2$ glass (black dotted line) taken from (Rai and Mountjoy 2014).

4. SiO$_2$–H$_2$O glasses quenched at high pressure

The presence of water in silica glass is typically only in parts-per-million quantities, but even this tiny amount has long been known to affect its' properties. A few percent water in silica can drastically affect both the density and viscosity of the melt. The structure of SiO_2 and H_2O are fundamental to our basic understanding of disordered materials, and are often used as archetypal examples of network formation and tetrahedral packing in glasses and liquids, respectively (Benmore 2012b). Silica and water have particular significance in the fields of geophysics and glass formation. From a liquid standpoint silica is a good glass former and so-called 'strong' liquid, using the terms of Angell (Angell 1995), indicating that the temperature dependence of the viscosity takes on an Arrhenius behavior. Water on the other hand, does not easily form a glass and can be considered a 'fragile' liquid since it's viscosity behavior deviates strongly from the Arrhenius relation. At high temperatures and pressures, above the critical point of $T_C \sim 1100\,°C$ and $P_C \sim 1$ GPa, water and silica are completely miscible, but below this point they separate into an aqueous fluid and silicate melt (Newton and Manning 2008, Mysen 2005). Such hydrothermal fluids are important in planetary processes on the Earth, terrestrial planets and in the outer Solar System. For example, on Earth fluid-rock interactions are known to dominate volcanic activity. Extracting the x-ray diffraction signal from such small, weakly scattering samples under these extreme conditions has previously proved difficult (Yamada *et al* 2011, Anderson *et al* 2014) until recently (Urakawa *et al* 2020).

On the basis of extensive infrared absorption and Raman studies, it has been suggested that at low concentrations water enters the silica network in the form of hydroxyl groups, however above about 7 wt.% evidence of molecular water starts to appear. This has led to a general model in which hydroxyl groups increase with increasing water content, and then remain constant at higher concentrations, at which point the amount of molecular water begins to increase linearly. A neutron and

x-ray study on 13 wt.% D_2O hydrous glass has shown separation into two phases; a major SiO_2 rich phase and a minor D_2O rich phase in small domains of <100 Å (Urakawa *et al* 2020). Despite this, little is known of how the hydroxyl groups effect the topology of the silicate network or the modification of the water structure within the pores of the glassy structure. Such information is important in understanding water solubility and diffusion mechanisms in geological magmas, the preparation of optical glass products and has relevance to the degradation of cements.

4.1. High pressure glasses experiment

Large volume (80 mg), high water content (up to 12 wt.%) samples of hydrous SiO_2 glass were synthesized at high pressures and temperatures using the multi-anvil laboratory at Arizona State University. In order to produce glasses with large amounts of H_2O, samples of $SiO_2 \sim 80$ mg in size were loaded into a 5 mm outer diameter platinum cup. Two samples were synthesized, one with ~ 8 wt.% and the other ~ 12 wt.% H_2O. Water was inserted into the cup with a syringe, and a platinum lid welded on to the top using a laser welder without allowing the H_2O to evaporate. The platinum can with the starting materials inside was loaded into a high pressure multi-anvil assembly and pressurized to 4 GPa. The temperature was raised to $1500\,°C$ using a graphite heater embedded in the high-pressure assembly and held for 1 h. The samples were then rapidly temperature-quenched to form a hydrous glass under pressure. A dual combination of Dexela detectors was used for the SAXS/WAXS measurement using an incident energy of 60 keV on beamline 6-ID-D at the APS (Benmore *et al* 2020b), with a similar x-ray diffraction set up and analysis procedure as described for the barium silicate experiment.

4.2. High pressure glasses results

The change in SAXS intensity with water content is shown in figure 9. The Porod index of the SAXS slope increases from $n \sim 0$ for dry SiO_2, to 0.83 for 8 wt.% H_2O and 3.3 for 12 wt.% H_2O. This indicates a change in roughness of the interface between the silica pores and water from irregular to smooth with increasing water content. There is also a very weak, broad peak encompassing $Q \sim 0.07$–0.12 Å^{-1} for the 8 wt.% H_2O–SiO_2 sample, suggesting a wide range of periodicities, possibly from ill-defined pores. This is in qualitative agreement with the results of (Urakawa *et al* 2020) that show heterogeneity over the length-scale of micrometers and a distribution of pore sizes. The high-Q region >3 Å^{-1} is similar between all three samples indicating that the SiO_4 unit is the dominant motif. Although, the 12 wt.% H_2O sample also contained some small superimposed Bragg peaks from remains of the platinum holder. The major difference between the dry glassy SiO_2 spectra and the SiO_2–H_2O glasses is the shift in position of the first sharp diffraction peak from $Q_{FSDP} = 1.53(1)$ to $1.71(1)$ Å^{-1}, see figure 10. This corresponds to a reduction in the periodicity associated with intermediate range ordering of the silicate network from $2\pi/Q_{FSDP} \sim 4.1$ to 3.7 Å.
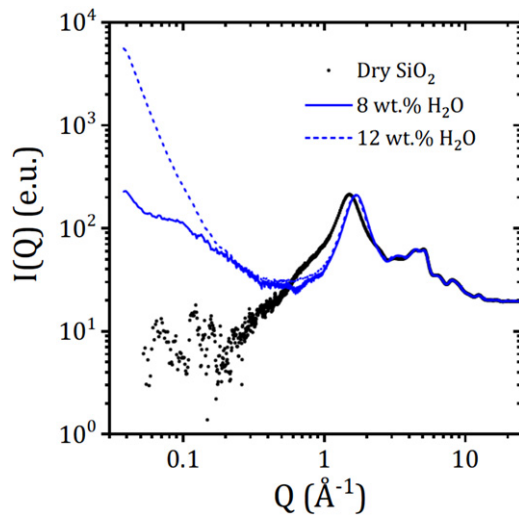
Figure 9. The normalized SAXS/WAXS intensity on a log-log plot for dry SiO_2 glass compared to the glasses synthesized at high pressure and temperature containing 8 wt.% and 12 wt.% water.
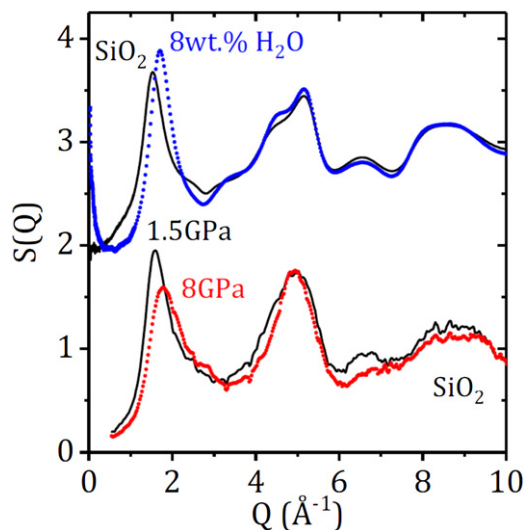

Figure 10. The x-ray structure factors of dry SiO_2 and 8 wt.% H_2O silicate glasses (shifted by +2) compared to those for dry SiO_2 glass measured in a diamond anvil cell at pressures of 1.5 and 8 GPa (Benmore *et al* 2010).

4.3. High pressure glasses discussion

It has been proposed that water causes a depolymerization of the silicate network in the melt which affects transport properties (Mysen 2005). The densification of network glasses at high pressures generally leads to a reduction in intermediate range order, which is manifested by a decrease in height of the FSDP (see figure 10) and a collapse of void space (and smaller ring sizes) corresponding to a shift of the FSDP to higher Q-values (Sampath *et al* 2003). It is therefore notable that the FSDP's in the SiO_2–H_2O glasses exhibit a slight increase in height, compared to that of dry SiO_2 glass, indicating the degree of order of the silicate network is maintained (or even enhanced) at high water contents >7 wt.% H_2O where pores
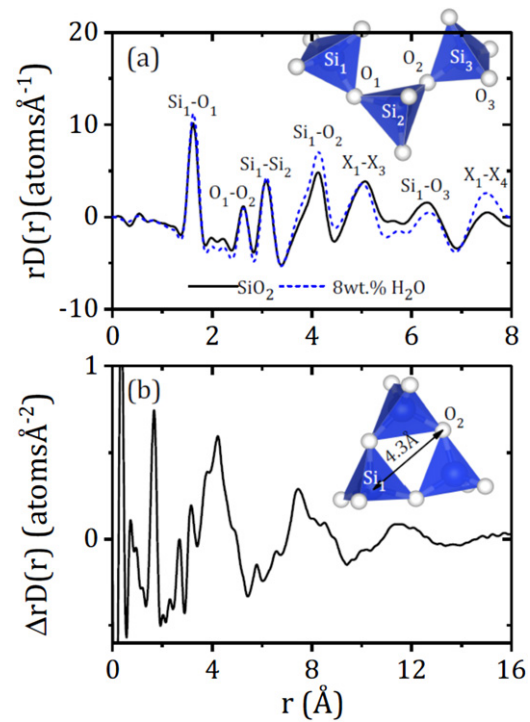

Figure 11. (a) The differential x-ray distribution function $D(r)$ multiplied by r, to emphasize the intermediate range order at longer distances for SiO_2 and 8 wt.% H_2O glasses. Atom−atom correlations are labeled based on the partial pair distribution functions of a corner shared SiO_2 glassy network (Mei *et al* 2008) where X−X corresponds to Si−Si and O−O. (b) The $rD(r)$ difference of the two curves shown in (a) and three corner-shared SiO_4 tetrahedra.

containing molecular water start to appear. Similar observations have been made by (Urakawa *et al* 2020) and have been linked to a decreasing Si−O−Si angle with pressure. X-ray diffraction data on water containing glasses (Zotov *et al* 1992) has also revealed increasing disorder with higher water contents leading to the presence of water-rich domains. Previous infra-red studies on multi-component hydrous alkali-silicate glasses suggest weak hydrogen bonding interactions between both hydroxyl and molecular water groups and silanols (Wu 1980, Acocella *et al* 1984, Bartholomew 1983).

Pure silica glass has a broad range of ring distributions, centered on six-fold rings of SiO_4 tetrahedra (Kohara and Suzuya 2005). The differential pair distribution functions, $D(r)$, of 8 and 12 wt.% H_2O–SiO_2 glasses show very similar features to that of the SiO_2 tetrahedral network, but with broad changes in relative intensity beyond the nearest neighbor tetrahedral interactions e.g. see figure 11. The 12 wt.% H_2O data are not shown due to the ambiguity introduced by the platinum contamination but yield essentially the same PDF as the 8 wt.% H_2O data. The difference between the SiO_2−H_2O and SiO_2 glasses isolates these broad correlations, which have a periodicity of ∼4 Å. The increase in intensity in $\Delta rD(r)$ at 4.3 Å is attributed to a growing number of Si_1−O_2 correlations, and the decrease around ∼6 Å due to the loss of Si_1−O_3 interactions. These changes are likely associated with the formation of three-membered rings of corner-shared SiO_4 tetrahedra, at the expense of larger rings. This is reasonable because three

fold rings are known to form in the melt at ambient pressure (McMillan *et al* 1994, Skinner *et al* 2013) and their number is expected to increase at higher pressures as the system densifies. However, this explanation needs to be verified by computer simulation, as the difference function comprises of changes in all atom-atom correlations i.e. the densified silica ring distribution (which appears to dominate), as well as water-water and water-silica interactions. Nonetheless, it is apparent that along with a slight distortion of the SiO_4 tetrahedra, the main changes in intermediate range ordering occur between distances of $\sim$3–18 Å. We therefore speculate that inhomogeneous clusters of corner shared three-membered SiO_4 rings occur in the high water content silicate glasses.

5. Summary and outlook

Two new hard x-ray methodologies for studying liquid, glassy and amorphous materials are discussed in this paper. The first is GI–PDF for analyzing grazing incidence high-energy x-ray data on amorphous thin films. This technique allows total structure factors to be measured out to high-Q values on films that are too thin to be measured in transmission geometry. The resulting $S(Q)$ over a wide Q-range provides high resolution PDF's compared to existing GI techniques. In the case of amorphous indium oxide, the data is shown to contain information of both the distribution of the local polyhedra as well as their connectivity. Namely, an approximate 1:2:3 ratio of face:corner:edge -sharing polyedhra was found in a heterogenous, low density In_2O_3 thin film. The second method is simultaneous high-energy SAXS/WAXS, which enables the ability to probe the local structure on an Angstrom scale, together with density fluctuations on the length-scale of a few tens of nanometers. When combined with high temperature and/or high pressure techniques the method allows the investigation of stable and metastable structures across phase diagrams. The examples of (i) homogenous liquid and two-phase glassy barium silicate indicate a Ba–O coordination number of 6–7 which supports the assertion that it is the weak ionic potential of Ba that leads to liquid-liquid immiscibility in the $BaO–SiO_2$ system. (ii) Changes in the medium range order of PDF data of heterogenous water-silica glasses produced at high pressures and temperatures, suggest the mechanism of densification is associated with the increase in the number of smaller ring sizes at the expense of larger ones. The analysis presented demonstrates the relative sensitivities of the SAXS/WAXS signal and the PDF to phase separation, and the changing topologies of melts upon quenching to the glassy state.

Indeed, both GI–PDF and high-energy SAXS/WAXS are well suited to the study of the types of inhomogeneous glassy networks described by Greaves (Greaves 1985, Greaves *et al* 1981, Greaves and Sen 2007, Bras *et al* 2003). The ability to probe wide regions of phase space over multiple length scales, will provide an essential database for the growing number of machine learning initiatives that are aimed at searching for 'global' interatomic potentials using large simulation boxes (Sivaraman *et al* 2020). X-ray PDF data on glassy and

amorphous materials provides a rigorous test of any interatomic potential and are critical for training simulated data sets designed to predict multiple structures and phase changes. Improvements in predictive capabilities of models is an important goal of applied glass science for development of functional glasses.

Data availability statement

The data that support the findings of this study are available upon reasonable request from the authors.

ORCID iDs

C J Benmore ⓘ https://orcid.org/0000-0001-7007-7749
G B González ⓘ https://orcid.org/0000-0002-1474-6095
O L G Alderman ⓘ https://orcid.org/0000-0002-2342-811X
S K Wilke ⓘ https://orcid.org/0000-0003-4674-7049
J K R Weber ⓘ https://orcid.org/0000-0002-2145-1279

References

Acocella J, Tomozawa M and Watson E B 1984 The nature of dissolved water in sodium silicate glasses and its effect on various properties *J. Non-Cryst. Solids* **65** 355–72
Anderson A J, Yan H, Mayanovic R A, Solferino G and Benmore C J 2014 High-energy x-ray diffraction of a hydrous silicate liquid under conditions of high pressure and temperature in a modified hydrothermal diamond anvil cell *High Press. Res.* **34** 100–9
Angell C A 1995 Formation of glasses from liquids and biopolymers *Science* **267** 1924–35
Bartholomew R F 1983 High-water containing glasses *J. Non-Cryst. Solids* **56** 331–42
Benmore C J 2012a A review of high-energy x-ray diffraction from glasses and liquids *ISRN Mater. Sci.* **2012** 1–19
Benmore C J 2012b A review of high-energy x-ray diffraction from glasses and liquids *ISRN Mater. Sci.* **2012** 1–19
Benmore C J *et al* 2020b Extended range X-ray pair distribution functions *Nucl. Instrum. Methods Phys. Res.* A **955** 163318
Benmore C J, Alderman O L G, Benmore S R, Wilke S K and Weber R J K 2020a Small-and wide-angle x-ray scattering studies of

liquid-liquid phase separation in silicate melts *ACS Earth Space Chem.* **4** 1888–94

Benmore C J, Soignard E, Amin S A, Guthrie M, Shastri S D, Lee P L and Yarger J L 2010 Structural and topological changes in silica glass at pressure *Phys. Rev.* B **81** 054105

Benmore C J and Weber J K R 2017 Aerodynamic levitation, supercooled liquids and glass formation *Adv. Phys.* X **2** 717–36

Bras W, Dolbnya I P, Detollenaere D, Van Tol R, Malfois M, Greaves G N, Ryan A J and Heeley E 2003 Recent experiments on a combined small-angle/wide-angle X-ray scattering beam line at the ESRF *J. Appl. Crystallogr.* **36** 791–94

Buchholz D B, Ma Q, Alducin D, Ponce A, Jose-Yacaman M, Khanal R, Medvedeva J E and Chang R P H 2014 The structure and properties of amorphous indium oxide *Chem. Mater.* **26** 5401–11

Buchholz D B, Zeng L, Bedzyk M J and Chang R P H 2013 Differences between amorphous indium oxide thin films *Prog. Nat. Sci.* **23** 475–80

Cormier L, Gaskell P H and Creux S 1999 Comparison of the low-Q features in diffraction data for silicate glasses and crystals containing Sr or Ba *J. Non-Cryst. Solids* **248** 84–91

Dippel A-C, Roelsgaard M, Boettger U, Schneller T, Gutowski O and Ruett U 2019 Local atomic structure of thin and ultrathin films via rapid high-energy x-ray total scattering at grazing incidence *Int. Union Crystallogr. J.* **6** 290–8

Egelstaff P A 1983 Many-body effects in the structure of water *Physica B+C* **120** 335–41

González G B, Okasinski J S, Buchholz D B, Boesso J, Almer J D, Zeng L, Bedzyk M J and Chang R P H 2017 Relationship between electrical properties and crystallization of indium oxide thin films using *ex-situ* grazing-incidence wide-angle x-ray scattering *J. Appl. Phys.* **121** 205306

Greaves G N 1985 EXAFS and the structure of glass *J. Non-Cryst. Solids* **71** 203–17

Greaves G N, Fontaine A, Lagarde P, Raoux D and Gurman S J 1981 Local structure of silicate glasses *Nature* **293** 611–6

Greaves G N and Sen S 2007 Inorganic glasses, glass-forming liquids and amorphizing solids *Adv. Phys.* **56** 1–166

Hammersley A P 2016 FIT2D: a multi-purpose data reduction, analysis and visualization program *J. Appl. Crystallogr.* **49** 646–52

Hasegawa H and Yasui I 1987 X-ray and neutron diffraction analyses of barium silicate glass *J. Non-Cryst. Solids* **95–96** 201–8

Hudon P and Baker D R 2002 The nature of phase separation in binary oxide melts and glasses. I. Silicate systems *J. Non-Cryst. Solids* **303** 299–345

Jensen K M Ø, Blichfeld A B, Bauers S R, Wood S R, Dooryhée E, Johnson D C, Iversen B B and Billinge S J L 2015 Demonstration of thin film pair distribution function analysis (tfPDF) for the study of local structure in amorphous and crystalline thin films *Int. Union Crystallogr. J.* **2** 481–9

Keen D A 2001 A comparison of various commonly used correlation functions for describing total scattering *J. Appl. Crystallogr.* **34** 172–7

Kohara S and Suzuya K 2005 Intermediate-range order in vitreous SiO₂ and GeO₂ *J. Phys. Condens. Matter.* **17** S77–86

Krogh-Moe J 1956 A method for converting experimental x-ray intensities to an absolute scale *Acta Crystallogr.* **9** 951–3

Levy H A, Danford M D and Narten A H 1966 Data collection and evaluation with an x-ray diffractometer designed for the study of liquid structure (Oak Ridge: Oak Ridge National Laboratory)

McGreevy R L and Pusztai L 1988 Reverse Monte Carlo simulation: a new technique for the determination of disordered structures *Mol. Simul.* **1** 359–67

McMillan P F, Poe B T, Gillet P H and Reynard B 1994 A study of SiO₂ glass and supercooled liquid to 1950 K via high-temperature Raman spectroscopy *Geochim. Cosmochim. Acta* **58** 3653–64

Mei Q, Benmore C J, Sen S, Sharma R and Yarger J L 2008 Intermediate range order in vitreous silica from a partial structure factor analysis *Phys. Rev.* B **78** 144204

Mysen B. R P 2005 *Silicate Glasses and Melts* 2nd edn (Amsterdam: Elsevier Science)

Narten A H 1972 Diffraction pattern and structure of noncrystalline BeF₂ and SiO₂ at 25 °C *J. Chem. Phys.* **56** 1905–9

Newton R C and Manning C E 2008 Thermodynamics of SiO₂–H₂O fluid near the upper critical end point from quartz solubility measurements at 10 kbar *Earth Planet. Sci. Lett.* **274** 241–9

Norman N 1957 The Fourier transform method for normalizing intensities *Acta Cryst.* **10** 370–3

Pacchioni G and Illas F 1995 Does the electronegativity scale apply to ionic crystals as to molecules? A theoretical study of the bonding character in molecular and crystalline alkaline-earth oxides based on dipole moments *Chem. Phys.* **199** 155–62

Pickup D, Moss R and Newport R 2014 NXFit: a program for simultaneously fitting x-ray and neutron diffraction pair-distribution functions to provide optimized structural parameters *J. Appl. Crystallogr.* **47** 1790–6

Qiu X, Thompson J W and Billinge S J L 2004a PDFgetX2: a GUI-driven program to obtain the pair distribution function from x-ray powder diffraction data *J. Appl. Crystallogr.* **37** 678

Qiu X, Thompson J W and Billinge S J L 2004b PDFgetX2: a GUI-driven program to obtain the pair distribution function from x-ray powder diffraction data *J. Appl. Crystallogr.* **37** 678

Rai M and Mountjoy G 2014 Molecular dynamics modelling of the structure of barium silicate glasses BaO–SiO₂ *J. Non-Cryst. Solids* **401** 159–63

Sampath S, Benmore C J, Lantzky K M, Neuefeind J, Leinenweber K, Price D L and Yarger J L 2003 Intermediate-range order in permanently densified [formula presented] glass *Phys. Rev. Lett.* **90** 115502

Seward T P, Uhlmann D R and Turnbull D 1968 Phase separation in the system BaO–SiO₂ *J. Am. Ceram. Soc.* **51** 278–85

Shannon R D and Prewitt C T 1970 Revised values of effective ionic radii *Acta Crystallogr.* B **26** 1046–8

Sinha S K, Sirota E B, Garoff S and Stanley H B 1988 X-ray and neutron scattering from rough surfaces *Phys. Rev.* B **38** 2297–311

Sivaraman G, Krishnamoorthy A N, Baur M, Holm C, Stan M, Csányi G, Benmore C and Vázquez-Mayagoitia Á 2020 Machine-learned interatomic potentials by active learning: amorphous and liquid hafnium dioxide *npj Comput. Mater.* **6** 104

Skinner L B, Benmore C J and Parise J B 2012 Area detector corrections for high quality synchrotron x-ray structure factor measurements *Nucl. Instrum. Methods Phys. Res.* A **662** 61–70

Skinner L B, Benmore C J, Weber J K R, Du J, Neuefeind J, Tumber S K and Parise J B 2014 Low cation coordination in oxide melts *Phys. Rev. Lett.* **112** 157801

Skinner L B, Benmore C J, Weber J K R, Wilding M C, Tumber S K and Parise J B 2013 A time resolved high energy x-ray diffraction study of cooling liquid SiO₂ *Phys. Chem. Chem. Phys.* **15** 8566–72

Soper A K 2005 Partial structure factors from disordered materials diffraction data: an approach using empirical potential structure refinement *Phys. Rev.* B **72** 104204

Soper A K and Barney E R 2011 Extracting the pair distribution function from white-beam X-ray total scattering data *J. Appl. Crystallogr.* **44** 714–26

Toby B H and Von Dreele R B 2013 GSAS-II: the genesis of a modern open-source all purpose crystallography software package *J. Appl. Crystallogr.* **46** 544–9

Tomlinson J W, Heynes M S R and Bockris J O M 1958 The structure of liquid silicates: Part 2. - molar volumes and expansivities *Trans. Faraday Soc.* **54** 1822–33

Urakawa S, Inoue T, Hattori T, Sano-Furukawa A, Kohara S, Wakabayashi D, Sato T, Funamori N and Funakoshi K-i 2020 X-ray and neutron study on the structure of hydrous SiO_2 glass up to 10 GPa *Minerals* **10** 84

Utsuno F *et al* 2006 Structural study of amorphous In2O3 film by grazing incidence x-ray scattering (GIXS) with synchrotron radiation *Thin Solid Films* **496** 95–8

Warren B E 1990 *X-ray Diffraction* (New York: Dover)

Waseda Y 1980 *The Structure of Non-crystalline Materials - Liquids and Amorphous* (New York: McGraw-Hill)

Weber J K R *et al* 2014 Measurements of liquid and glass structures using aerodynamic levitation and in-situ high energy x-ray and neutron scattering *J. Non-Cryst. Solids* **383** 49–51

Wright A C 1994 Neutron scattering from vitreous silica. V. The structure of vitreous silica: what have we learned from 60 years of diffraction studies? *J. Non-Cryst. Solids* **179** 84–115

Wu C-K 1980 Stable silicate glasses containing up to 10 weight percent of water *J. Non-Cryst. Solids* **41** 381–98

Yamada A, Inoue T, Urakawa S, Funakoshi K-i, Funamori N, Kikegawa T and Irifune T 2011 In situ x-ray diffraction study on pressure-induced structural changes in hydrous forsterite and enstatite melts *Earth Planet. Sci. Lett.* **308** 115–23

Zanotto E D, James P F and Craievich A F 1986 The effects of amorphous phase separation on crystal nucleation kinetics in BaO–SiO_2 glasses—Part 3 Isothermal treatments at 718 to 760 °C; small-angle x-ray scattering results *J. Mater. Sci.* **21** 3050–64

Zotov N, Yanev Y, Epelbaum M and Konstantinov L 1992 Effect of water on the structure of rhyolite glasses—x-ray diffraction and Raman spectroscopy studies *J. Non-Cryst. Solids* **142** 234–46